J. Fluid Mech. (1989), *vol.* 199, *pp.* 1–28
Printed in Great Britain

Numerical simulation of thermal convection in a two-dimensional finite box

By ISAAC GOLDHIRSCH†, RICHARD B. PELZ‡ AND STEVEN A. ORSZAG§

† Department of Fluid Mechanics and Heat Transfer, Faculty of Engineering, Tel-Aviv University Ramat-Aviv, Tel-Aviv 69978, Israel

‡ Department of Mechanical and Aerospace Engineering, Rutgers University, PO Box 909, Piscataway, NJ 08855, USA

§ Applied and Computational Mathematics, Princeton University, Princeton, NJ 08544, USA

(Received 22 October 1986 and in revised form 24 February 1988)

The problems of dynamical onset of convection, textural transitions and chaotic dynamics in a two-dimensional, rectangular Rayleigh–Bénard system have been investigated using well-resolved, pseudo-spectral simulations. All boundary conditions are taken to be no-slip. It is shown that the process of creating the temperature gradient in the system, is responsible for roll creation at the side boundaries. These rolls either induce new rolls or move into the interior of the cell, depending on the rate of heating. Complicated flow patterns and textural transitions are observed in both non-chaotic and chaotic flow regimes. Multistability is frequently observed. Intermediate-Prandtl-number fluids (e.g. 0.71) have a quasi-periodic time dependence up to Rayleigh numbers of order 10^6. When the Prandtl number is raised to 6.8, one observes aperiodic (chaotic) flows of non-integer dimension. In this case roll merging and separation is observed to be an important feature of the dynamics. In some cases corner rolls are observed to migrate into the interior of the cell and to grow into regular rolls; the large rolls may shrink and retreat into corners. The basic flow patterns observed do not change qualitatively when the chaotic regime is entered.

1. Introduction

In recent years, there has been a growing interest in the dynamics of the Rayleigh–Bénard system (Chandrasekhar 1961). Improved experimental techniques, most notably, laser-Doppler velocimetry (Gollub & Benson 1980) and high-speed data collection techniques have revealed a rich spectrum of flow patterns and states. Advances in the theory of dynamical systems have led to the prediction of universal routes to chaos (see examples in Cvitanovic 1984) which have been observed experimentally (cf. Libchaber & Maurer 1980; Giglio, Musazzi & Perini 1981). Analytical methods based on the amplitude expansion approach and variational principles (e.g. Newell & Whitehead 1969; Segel 1969; Cross *et al.* 1980; Cross 1982*a*; Greenside *et al.* 1982; Zippelius & Siggia 1982; Cross *et al.* 1983*a*; Cross & Newell 1984) have been employed to investigate parts of the observed phenomena. Last, but not least, numerical simulations (e.g. Moore & Weiss 1973; Siggia & Zippelius 1981; McLaughlin & Orszag 1982; Grötzbach 1982; Grötzbach 1983; Curry *et al.* 1984; Yahata 1984) have been performed in an effort to elucidate the dynamics of the Rayleigh–Bénard system.

One of the main reasons the Rayleigh–Bénard system is of such wide interest is that it has a gradual transition to chaos, which can be carefully studied and compared to theoretical predictions (at least for low-aspect-ratio systems). Such transitions are typical of low-order, dynamical systems.

The theory of dynamical systems concerns itself mainly with the investigation of coupled sets of ordinary, nonlinear, first-order-in-time differential equations (Guckenheimer & Holmes 1983). The disadvantage of this method as far as the Rayleigh–Bénard system is concerned is an obvious lack of connection to the Navier–Stokes equations describing the dynamics of fluids. The advantage of dynamical systems is their relative simplicity and the wealth of universal results (Cvitanovic 1984) one can obtain through their analysis (or through the analysis of recursion relations that represent Poincaré sections of the solutions to such differential equations). In the cases where typical results of the theory of dynamical systems are observed in hydrodynamic systems, there are only a small number of relevant modes and the chaotic behaviour would typically be termed 'weak turbulence'.

The chief assumption involved in the method of 'amplitude equations' (Newell & Whitehead 1969; Segel 1969) is the existence of some slow space and timescales in the problem. Such a slow scale is described by a small parameter ϵ measuring the closeness to the first instability (e.g. $\epsilon = (R-R_c)/R_c$ in the case of Bénard convection). Consequently, the validity of the resulting equations is limited, at least in principle, to the close vicinity of the first instability. In practice, amplitude equations seem to be valid up to $\epsilon = O(1)$ in some cases. Claims have also been made by Greenside, Coughran & Schryer (1982) that amplitude equations contain enough information to describe many aspects of the chaotic states.

An interesting approach to the dynamics of the Rayleigh–Bénard system (and other systems) is the use of truncated sets of modes (Lorenz 1963; Curry 1978). In this case, spurious chaotic solutions may be obtained (Curry *et al.* 1984). This may also happen for amplitude equations used beyond their region of validity. One of the reasons for the appearance of such spurious chaotic solutions is the neglect of high wavenumber modes, where most of the dissipation takes place.

Since solutions to the Navier–Stokes equations are far richer in structure and flow states than any of the above methods seem to predict, there may be no substitute for a direct numerical investigation. In most numerical and analytical treatments of the Rayleigh–Bénard system, convenient boundary conditions have been chosen, e.g. periodic and stress-free boundary conditions (Moore & Weiss 1973; McLaughlin & Orszag 1982; Curry *et al.* 1984).

Computing power and numerical methods at present available are sufficient for performing resolved simulations of at least two-dimensional convection with realistic boundary conditions. By two-dimensional, we mean the domain has one vertical and one horizontal dimension. We believe such simulations are an important means, as are similar simulations of other systems, of learning about the detailed dynamics of convection and obtaining an intuition about the processes that govern the convective dynamics. They also serve to extract detailed quantitative data. The results obtained this way should be helpful in any attempt to construct a theory for thermal convection.

The relevance of studies of two-dimensional convection may be questioned since systems in nature are basically three-dimensional. Many flows in three-dimensional systems have, however, a two-dimensional nature; parallel rolls are one example. Many three-dimensional states result from instabilities of corresponding two-

dimensional states (Busse 1978). In other types of flows one has a similar situation; e.g. the instability of two-dimensional travelling waves in shear flow to three-dimensional disturbances (Orszag & Patera 1983). Three-dimensional magneto-hydrodynamic convection in a strong magnetic field is essentially equivalent to two-dimensional convection (Busse 1978). It is also believed that many large-scale processes in the atmosphere are essentially two-dimensional. Thus the investigation of model two-dimensional equations provides us with both physical insight into some of the flow processes and a testing ground for dynamical system theory and numerical methods. However, we know of no experimental system which corresponds directly to the two-dimensional Boussinesq equations for Rayleigh–Bénard convection.

The structure of the paper is as follows. In §2 we present the Boussinesq equations and the boundary conditions. We also describe the numerical method. In §3 we present a detailed account of the low-Rayleigh-number results. In §4 the results for intermediate Rayleigh numbers are displayed. In §5 we report the results of simulations for high Rayleigh numbers. All of the above simulations are for a Prandtl number of 0.71. In §6 we present the dynamics of the Rayleigh–Bénard system for a Rayleigh number of 100000, a Prandtl number of 6.8 and an aspect ratio of 2, as an example of possible chaotic dynamics. More details of the chaotic dynamics in the two-dimensional Rayleigh–Bénard system are reserved for a future publication. Section 7 offers a short summary of the results and relates to future work.

2. Equations and numerical methods

In §2.1 we formulate the problem of convection in a rectangle whose boundaries are assumed to be perfect conductors. In §2.2 we describe the numerical methods used.

2.1. *The Boussinesq equations*

Since many fluids, especially liquids, are only very weakly compressible, one is justified in assuming that the density of the fluid is a function of the temperature alone. In the range of temperature differences relevant to the Rayleigh–Bénard problem, such a dependence may be assumed linear. These approximations form the essence of the Boussinesq approximation, which is well known to yield a successful model for many convection problems (Boussinesq 1903; Busse 1978).

We consider a fluid contained in a rectangle of width L and height D with perfectly conducting boundaries. The rectangle is defined as the region $0 \leqslant z \leqslant D, 0 \leqslant x \leqslant L$. The gravitational field is in the negative z-direction. The aspect ratio, Γ, is defined as L/D.

The Boussinesq equations are:

$$\frac{\partial \boldsymbol{v}}{\partial t} = \boldsymbol{v} \times \boldsymbol{\omega} - \frac{1}{\rho} \boldsymbol{\nabla}(P + \tfrac{1}{2}v^2) + \alpha g T \hat{\boldsymbol{z}} + \nu \Delta \boldsymbol{v}, \tag{2.1}$$

$$\frac{\partial T}{\partial t} + \boldsymbol{v} \cdot \boldsymbol{\nabla} T = \kappa \Delta T, \tag{2.2}$$

$$\boldsymbol{\nabla} \cdot \boldsymbol{v} = 0, \tag{2.3}$$

where $\boldsymbol{v} = (v_x, v_z)$ is the velocity field, $\boldsymbol{\omega} = \boldsymbol{\nabla} \times \boldsymbol{v}$ the vorticity field, T the temperature field, P the pressure, ν the kinematic viscosity, α the coefficient of thermal expansion,

κ the coefficient of heat conductivity, ρ the mass density, t the time and g the gravitational acceleration. Equation (2.3) expresses the condition of incompressibility. The boundaries are assumed to be perfect conductors. The temperatures of the top and bottom boundaries are given functions of time. The term $\alpha T\hat{z}$ in (2.1) may be changed by the gradient of a function at will, since the difference can be absorbed into the 'pressure'. Thus we assume that the temperature of the top plate, $z = D, 0 \leqslant x \leqslant L$, is zero. The temperature of the bottom plate, $T_{\text{bot}}(t)$ ($z = 0$, $0 \leqslant x \leqslant L$), is assumed to be uniform and time dependent. We define now an 'instantaneous' temperature field $T_{\text{inst}}(t, z)$:

$$T_{\text{inst}}(t, z) = T_{\text{bot}}(t)\left(1 - \frac{z}{d}\right). \tag{2.4}$$

T_{inst} is just a linear interpolation of the temperature between the two horizontal boundaries. We assume that $T = T_{\text{inst}}$ on the sidewalls:

$$T = T_{\text{inst}} \quad \text{when } x = 0, L \quad \text{for } 0 \leqslant z \leqslant D. \tag{2.5}$$

Now we define

$$T^* = T - T_{\text{inst}}, \quad \delta = \lim_{t \to \infty} T_{\text{bot}}(t), \quad \theta = T^*/\delta, \quad \theta_{\text{inst}} = T_{\text{inst}}/\delta.$$

Now we rescale the variables in (2.1)–(2.3) as follows: lengths are scaled by D, time by D^2/κ (thermal diffusion time) and temperature by δ. Let $Ra = g\alpha D^3\delta/\nu\kappa$ and $Pr = \nu/\kappa$ be the Rayleigh and Prandtl numbers respectively. The rescaled velocities and vorticity are still called $\boldsymbol{v}$ and $\boldsymbol{\omega}$, respectively. The rescaled independent variables will be called x, z and t as before. The resulting equations are:

$$\frac{\partial \boldsymbol{v}}{\partial t} = \boldsymbol{v} \times \boldsymbol{\omega} - \boldsymbol{\nabla}\pi + Ra\, Pr\, \theta\hat{z} + Pr\, \Delta \boldsymbol{v}, \tag{2.6}$$

where π contains all 'potential' terms, and

$$\frac{\partial \theta}{\partial t} + \boldsymbol{v} \cdot \boldsymbol{\nabla}\theta = -\boldsymbol{v} \cdot \boldsymbol{\nabla}\theta_{\text{inst}} - \dot{\theta}_{\text{inst}} + \Delta\theta, \tag{2.7}$$

$$\boldsymbol{\nabla} \cdot \boldsymbol{v} = 0. \tag{2.8}$$

The rescaled boundary conditions then are:

$$\boldsymbol{v} = \theta = 0 \quad \text{on } z = 0, 1 \quad (0 \leqslant x \leqslant \Gamma), \tag{2.9a}$$

$$\text{on } x = 0 \quad (0 \leqslant z \leqslant 1), \tag{2.9b}$$

$$\text{on } x = \Gamma \quad (0 \leqslant z \leqslant 1), \tag{2.9c}$$

(the last two conditions expressing the perfect conductivity of the sidewalls). The actual rescaled temperature at any point is $\theta + \theta_{\text{inst}}$, where

$$\theta_{\text{inst}} = (1 - z)\, \theta_{\text{inst}}(z = 0, t). \tag{2.10}$$

Finally, in the heating process we choose for simplicity:

$$\theta_{\text{inst}}(z = 0, t) = 1 - \exp(-t/\bar{t}), \tag{2.11}$$

where $\bar{t}$ is a chosen timescale.

Upon substituting (2.10) and (2.11) into (2.7), we obtain:

$$\frac{\partial\theta}{\partial t}+\boldsymbol{v}\cdot\boldsymbol{\nabla}\theta = v_z(1-\exp(-t/\bar{t})-\frac{1}{\bar{t}}\exp(-t/\bar{t})+\Delta\theta. \tag{2.12}$$

Equations (2.6), (2.8) and (2.12) are the equations of motion to be solved, subject to the boundary conditions given by (2.9).

The equations of motion, as described so far, possess right–left symmetry: when $v_x(x,z)$ is replaced by $-v_x(\Gamma-x,z)$, $v_z(x,z)$ is replaced by $v_z(\Gamma-x,z)$ and $\theta(x,z)$ is replaced by $\theta(\Gamma-x,z)$, the equations remain invariant. Consequently if the system is prepared by a heating process which satisfies this symmetry, the resulting flow states will be symmetric with respect to reflections about the vertical centre line. The type of heating which is suggested in (2.11) possesses this property. Since the states obtained by such a heating process may be unstable to infinitesimal or finite perturbations that break this symmetry, we have also considered an asymmetric perturbation which can give rise to final asymmetric states. The perturbation we use is of the form:

$$\delta\theta = \beta\exp\{-[(x-x_0)^2+(z-z_0)^2]/C\}, \tag{2.13}$$

where C, x_0, z_0, and β are parameters that fix the width, location, and strength of the perturbation respectively. As is shown in the following sections, such a perturbation suffices to induce asymmetrical states.

Another symmetry of interest possessed by the equations of motion (for steady states) is an overall rotation by π radians. The corresponding transformation is:

$$v_x^*(x,z) = -v_z(\Gamma-x,1-z),\quad v_z^*(x,z) = -v_x(\Gamma-x,1-z),\quad \theta^*(x,z) = -\theta(\Gamma-x,1-z), \tag{2.14a–c}$$

where the $(\,)^*$ denotes the transformed fields. We have found that many steady flow fields obey this symmetry, even when the left–right symmetry is broken.

When one combines the left–right symmetry and the 'π' symmetry, one obtains a symmetry transformation, the 'top–bottom' symmetry, which changes the sense of rotation of the rolls. This transformation is defined as follows:

$$v_x^*(x,z) = v_x(x,1-z),\quad v_z^*(x,z) = -v_z(x,1-z),\quad \theta^*(x,z) = -\theta(x,1-z). \tag{2.15a–c}$$

Note that when the rolls are not symmetric with respect to the horizontal centreline (which is the case for most Rayleigh numbers) changing the sense of rotation actually implies a change in pattern.

We stress that the left–right symmetry is a symmetry of the full dynamical equations of motion whereas the 'π' rotation and the 'top–bottom' reflection symmetry apply only to the steady state.

2.2. *The numerical methods*

In this subsection we describe the numerical methods used to solve the Boussinesq equations (2.6)–(2.8). First, we describe the spatial approximation scheme and then the time integration scheme.

The pseudo-spectral method (Gottlieb & Orszag 1977) is used for spatial discretization. The dependent variables, v and θ, are expressed as

$$\begin{Bmatrix} v_x \\ v_z \\ \theta \end{Bmatrix}(x,z,t) = \sum_{m=0}^{M}\sum_{n=0}^{N} \begin{Bmatrix} \hat{v}_x \\ \hat{v}_z \\ \hat{\theta} \end{Bmatrix}(m,n,t)\, T_m\left(\frac{2x}{\Gamma}-1\right) T_n(2z-1), \tag{2.16}$$

where $T_m(s)$ is the mth degree Chebyshev polynomial defined by $T_m(s) = \cos[m \cos^{-1}(s)]$.

The pseudo-spectral method is a collocation method based on the representation (2.16) with collocation points:

$$x_m = \tfrac{1}{2}\Gamma\left[\cos\left(\frac{\pi m}{M}\right)+1\right], \quad z_n = \tfrac{1}{2}\left[\cos\left(\frac{\pi n}{N}\right)+1\right]. \tag{2.17a, b}$$

If the function to be approximated is analytic, the convergence of this pseudo-spectral approximation is exponential as M and N increase. The set of collocation points (2.17) is clustered near the boundaries where boundary layers are expected.

Equation (2.16) is an expression for an interpolating polynomial at the points given in (2.17). The terms in the Boussinesq equations are calculated at each of the interpolation points. An accurate expression for a partial derivative can be derived from (2.16) and the recursion relation for Chebyshev polynomials. In one dimension the exact expression for the derivative has the form:

$$\frac{\mathrm{d}}{\mathrm{d}x} v(x) = \frac{\mathrm{d}}{\mathrm{d}x} \sum_{m=0}^{\infty} \hat{v}(m)\, T_m(x) = \sum_{m=0}^{\infty} b(m)\, T_m(x), \tag{2.18a}$$

$$c(n-1)\, b(n-1) - b(n+1) = 2n\hat{v}(n) \quad \text{for } n \geqslant 1, \tag{2.18b}$$

where $c(0) = 2$ and $c(n) = 1$ for $n \geqslant 1$. The derivative of the finite series expansion can be calculated with a truncated version of (2.18). Fast Fourier transform methods provide an efficient way to transform a field of physical variables to the corresponding Chebyshev coefficients.

Using this pseudo-spectral spatial approximation, the Boussinesq equations are reduced to a system of first-order, ordinary differential equations in time for the velocity and temperature at each collocation point. The time integration of the system is accomplished by 'splitting' the equation into parts; the nonlinear terms are advanced by an explicit scheme, and the linear terms are advanced by an implicit scheme.

In the explicit step a second-order, Adams–Bashforth scheme is used to advance the nonlinear terms:

$$\frac{\boldsymbol{v}^* - \boldsymbol{v}^n}{\Delta t} = \tfrac{3}{2}(\boldsymbol{v}\times\boldsymbol{\omega} + Ra\, Pr\, \theta\hat{z})^n - \tfrac{1}{2}(\boldsymbol{v}\times\boldsymbol{\omega} + Ra\, Pr\, \theta\hat{z})^{n-1}, \tag{2.19a}$$

$$\frac{\theta^* - \theta^n}{\Delta t} = -\tfrac{3}{2}(\boldsymbol{v}\cdot\nabla\theta + \boldsymbol{v}\cdot\nabla\theta_{\mathrm{inst}} + \dot{\theta}_{\mathrm{inst}})^n + \tfrac{1}{2}(\boldsymbol{v}\cdot\nabla\theta + \boldsymbol{v}\cdot\nabla\theta_{\mathrm{inst}} + \dot{\theta}_{\mathrm{inst}})^{n-1}, \tag{2.19b}$$

where the superscript n refers to time level n.

After this essentially inviscid step, the flow field is not incompressible. The pressure is then used to enforce incompressibility. A Poisson equation for the pressure is obtained by taking the divergence of the momentum equation. Assuming that $\boldsymbol{v}^n$ is incompressible, the equation for the pressure is:

$$\Delta\pi = \nabla\cdot\boldsymbol{v}^*/\Delta t. \tag{2.20}$$

The Laplacian in (2.20) can be split into an $M \times M$ matrix for the second derivative in the x-direction and an independent $N \times N$ matrix for the second derivative in the z-direction (Haidvogel & Zang 1979). In a preprocessing step, the inverses of these matrices are computed using an eigenvalue/vector decomposition. The boundary conditions are taken to be $\partial\pi/\partial n = 0$ at all boundaries, which preserves consistency of the dependent variables but results in an $O(\Delta^0)$ error in the divergence of the velocity at the boundary. This error is decreased by the improved pressure boundary conditions introduced in §7.1.2 of Orszag, Israeli & Deville (1986).

The intermediate velocity field is made solenoidal by subtracting the gradient of the pressure from the result of (2.19*a*):

$$\frac{\boldsymbol{v}^{**} - \boldsymbol{v}^{*}}{\Delta t} = \nabla\pi. \tag{2.21}$$

The variables are then updated to the $(n+1)$ time level by employing the implicit, Crank–Nicholson scheme on the remaining viscous terms:

$$\frac{\boldsymbol{v}^{n+1} - \boldsymbol{v}^{**}}{\Delta t} = \tfrac{1}{2}Pr\,\Delta(\boldsymbol{v}^{n+1} + \boldsymbol{v}^{**}), \quad \frac{\theta^{n+1} - \theta^{**}}{\Delta t} = \tfrac{1}{2}\Delta(\theta^{n+1} + \theta^{**}), \tag{2.22a, b}$$

with homogeneous boundary conditions. In the preprocessing step the Laplacian is decomposed in a way similar to the pressure.

Approximately 80% of the CPU time for each timestep is spent doing 8 matrix multiplications necessary for inversion of the Laplacians. A calculation with a grid of 32^2 points takes about 0.1 s/timestep on a Cray 1 computer.

3. Low Rayleigh number behaviour: $Ra < 10^4$

In this section we present results for Rayleigh numbers less than twice the critical Rayleigh number, e.g. $Ra \leqslant 10000$ for $\Gamma = 1$. Both the onset of convection and the subsequent dynamics are described.

The Rayleigh–Bénard instability is triggered by heating the lower horizontal plate in a time dependent fashion (see §2.1). For any rate of heating and for all Rayleigh numbers (including $Ra < Ra_c$) the heating process creates rolls at the boundaries. In figure 1 (*a*, *b*) we show an example of slow heating to a subcritical Rayleigh number, $Ra = 2000$. Here $\bar{t} = 1$ (cf. (2.11)) and $\Gamma = 2$. The distortion of the temperature field due to the heating process and the resulting rolls at the sidewalls are prominent at this very early time $t = 0.01$. Similar sidewall roll development occurs at all subcritical Rayleigh numbers (checked for Rayleigh numbers as low as 10). When the system is heated to a final Rayleigh number below the critical one, the rolls eventually decay. The physical mechanism responsible for the creation of the rolls is obvious: due to the difference in thermal diffusivities between the fluid and the sidewalls (the latter are assumed to be perfect conductors), a horizontal component of the temperature gradient is created close to the boundaries. As is well known, when the temperature gradient has a component which is orthogonal to the gravitational field, the fluid is unstable (for any 'size' of this component). The result is roll creation. In contrast to the model suggested by Ahlers & Behringer (1978) and Ahlers *et al.* (1981), but consistent with Cross, Hohenberg & Lücke (1983), no noise or (uncontrolled) external perturbation of any kind is necessary to trigger the onset of the instability.

Following its creation at the wall, the roll moves into the interior of the cell. This

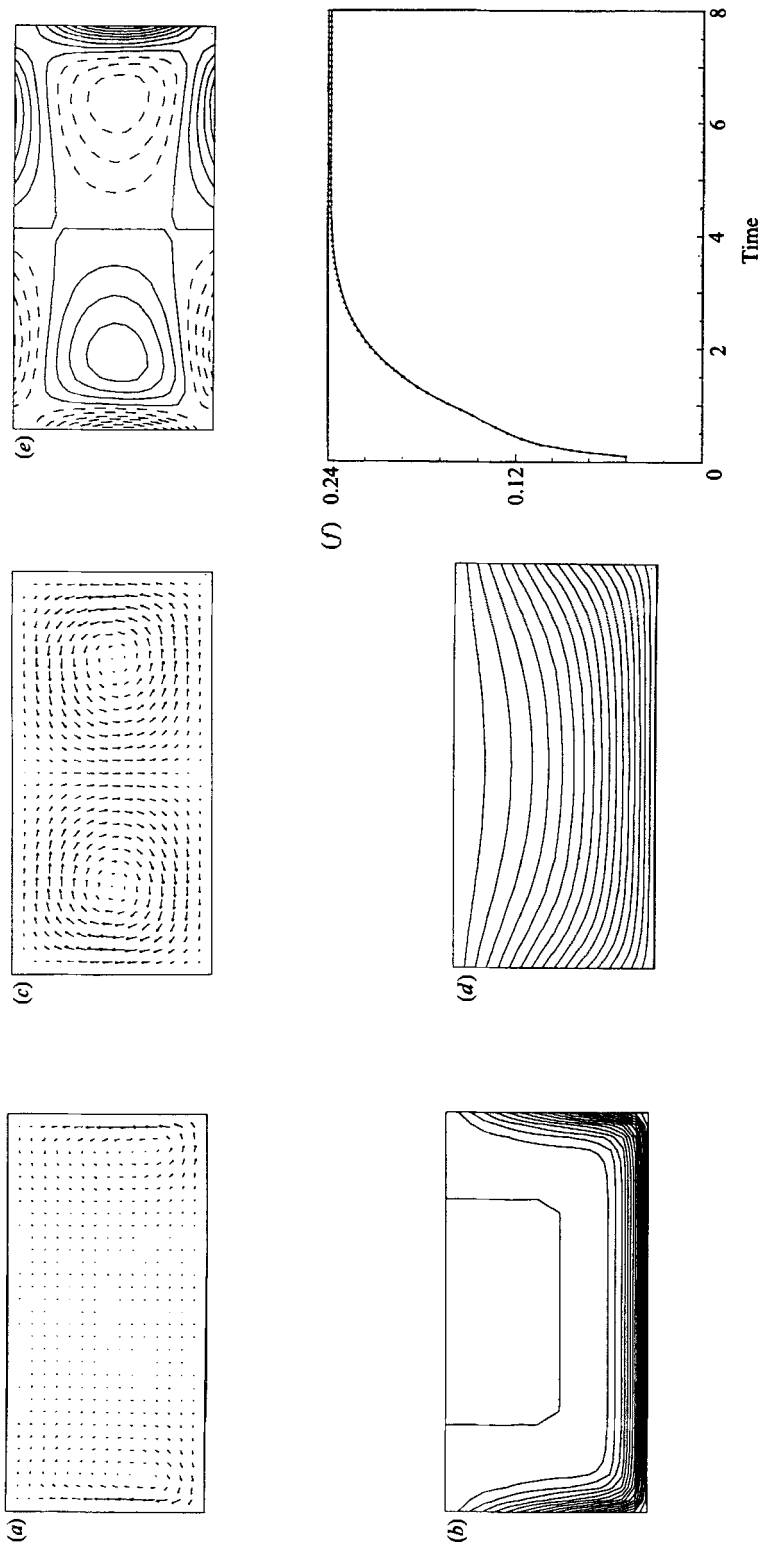

FIGURE 1. (*a*) Velocity vector plot for $R = 2000$, $\Gamma = 2$, $Pr = 0.71$, $t = 1$ at a time of 0.01. (*b*) The temperature contours corresponding to (*a*). (*c*) The velocity vector plot at a time of 0.2. (*d*) The temperature contour plot corresponding to (*c*). (*e*) The vorticity contour plot corresponding to (*c*). (*f*) The position of the roll centre as a function of time.

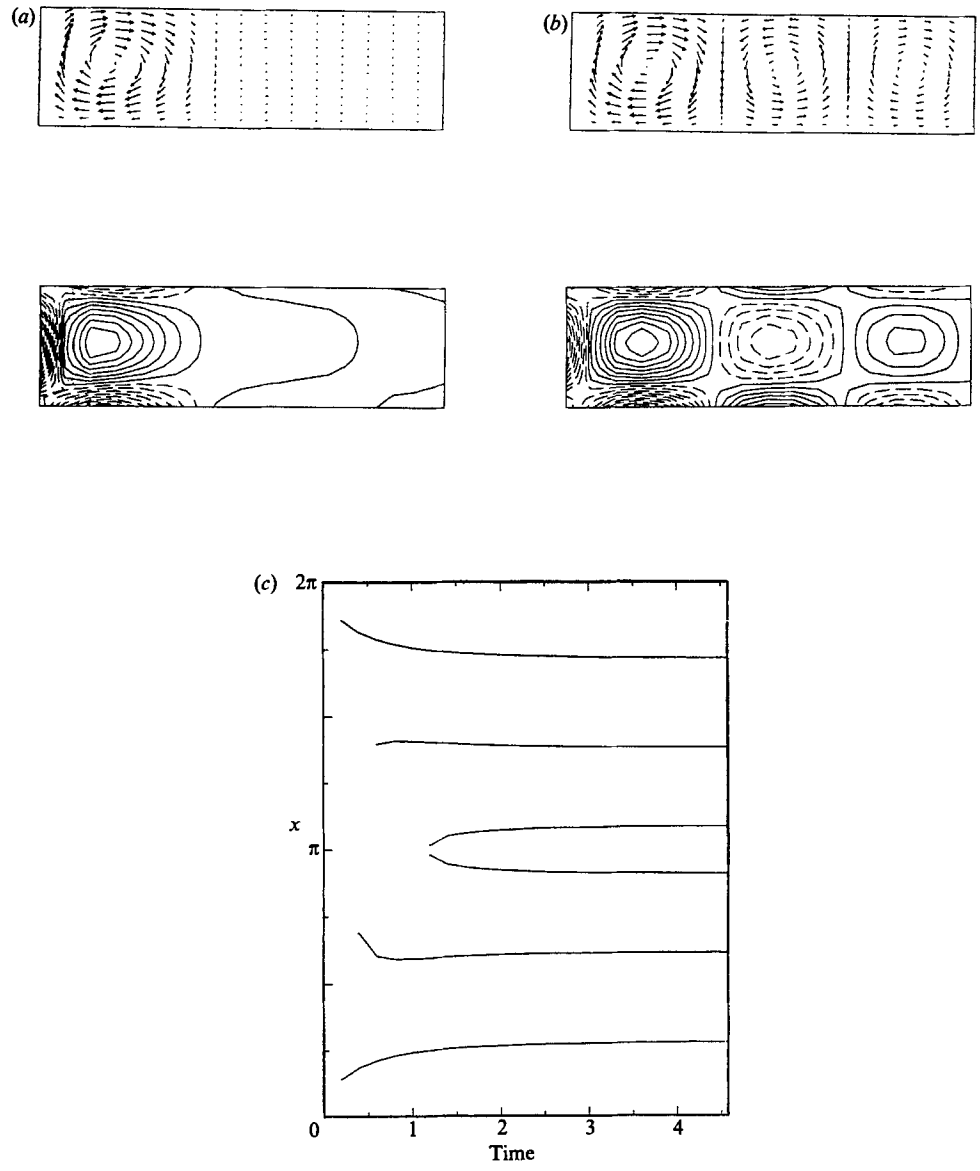

FIGURE 2. Induction of new rolls by the primary roll. The parameters are: $R = 1500$, $\Gamma = 2\pi$ and $Pr = 0.71$. Only the left half of the cell is shown; the right half is a mirror image. Velocity vector plots (upper figures) as well as vorticity contour plots are shown for the times: (*a*) time of 1; (*b*) time of 6. (*c*) The positions of the various rolls in the cell as a function of time.

effect is also demonstrated in figure 1. In figure 1 (*c–e*) the rolls created at the sidewalls have moved into the interior of the box. Here again we note the large distortion in the temperature field that was initially created in the heating process. At a later time we observe a less distorted field. Note the strong boundary layer at the sidewalls as may be seen in the vorticity plot in figure 1 (*e*). Firstly, these rolls move in at an (almost) constant velocity, and then they stop moving. In figure 1 (*f*) we plot the position of the right-most roll, following its creation at a time $t = 0$. This position was defined as the position of the extremum of the vorticity in the roll.

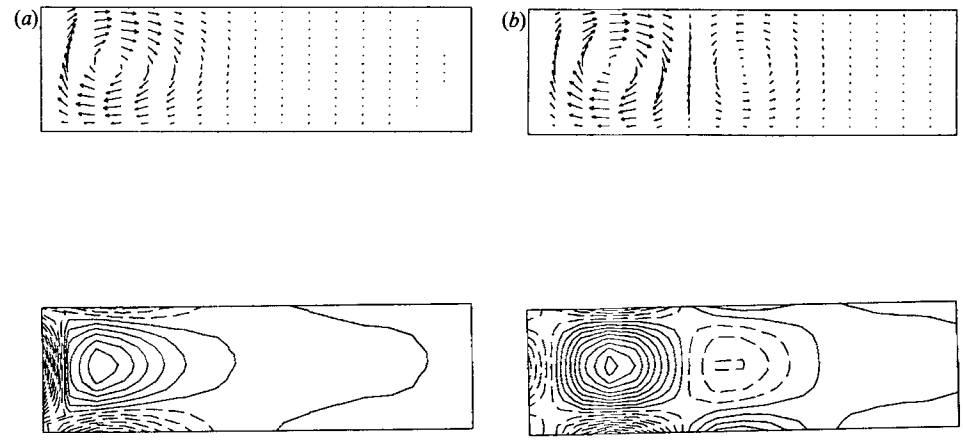

FIGURE 3. (a) Velocity vector plot for: $R = 1650$, $Pr = 0.71$, $\Gamma = 2\pi$, $\bar{t} = 1$ and a time of 0.35. The lower figure is the corresponding vorticity contour plot. Only the left half of the cell is shown. (b) Same plots as in (a) for $\bar{t} = 0.05$.

Note the slowing down of the roll as it approaches its 'final' position and the relatively large time ($t \approx 4$) it takes to attain this position.

In cells of large aspect ratios, more rolls are subsequently created in the interior of the cell. The existence of these latter cells is induced by the primary rolls which are created at the sidewalls. Figure 2(a, b) demonstrates this phenomenon for a cell aspect ratio of 2π and $Ra = 1500$ (only half a cell is shown, the other half being a mirror image of the first). Figure 2(a) shows the creation of the roll ($\bar{t} = 1$); the corresponding vorticity plot reveals the existence of a single roll. A secondary roll is induced by the parent roll at a later time. In figure 2(b) one observes three rolls. We reiterate that all of this is happening below the critical Rayleigh number. In figure 2(c) we present the time-dependent positions of these rolls from the moment of their creation.

When the Rayleigh number is subcritical, the convective structure eventually decays at an asymptotic rate that corresponds to the one predicted by the linearized Boussinesq equations. Above the critical Rayleigh number the rolls stabilize to create a steady convective state. For example, at a Rayleigh number at 7000 and aspect ratio of 2, 'square-like' patterns of two convecting rolls are developed (in order to 'fit' in the container). Such rolls were predicted by Busse & Frick (1985) for the case of temperature-dependent viscosity.

The rate of initial heating of the bottom plate is important in determining the dynamics of the onset. In figure 3(a) we show the velocity and vorticity fields at a time of 0.35 for a box with an aspect ratio of 2π (only the left half of the box is shown) at a Rayleigh number of 1650 and $\bar{t} = 1$ (cf. (2.11)). No induced roll is visible. The maximal value of the velocity field is approximately 0.7 in dimensionless units. On the other hand, when $\bar{t} = 0.05$, we observe a secondary roll and the maximal velocity is about 2.4 (see figure 3b). When the heating is fast, the primary roll has a fast rotation rate which creates a relatively large shear stress. The latter induces a secondary roll. At a later time, $t = O(1)$, even the slow heating rate causes the creation of an induced roll, as seen in figure 2.

An interesting phenomenon occurs when the steady state of the system consists of an odd number of rolls. The heating process, being symmetric to reflection through

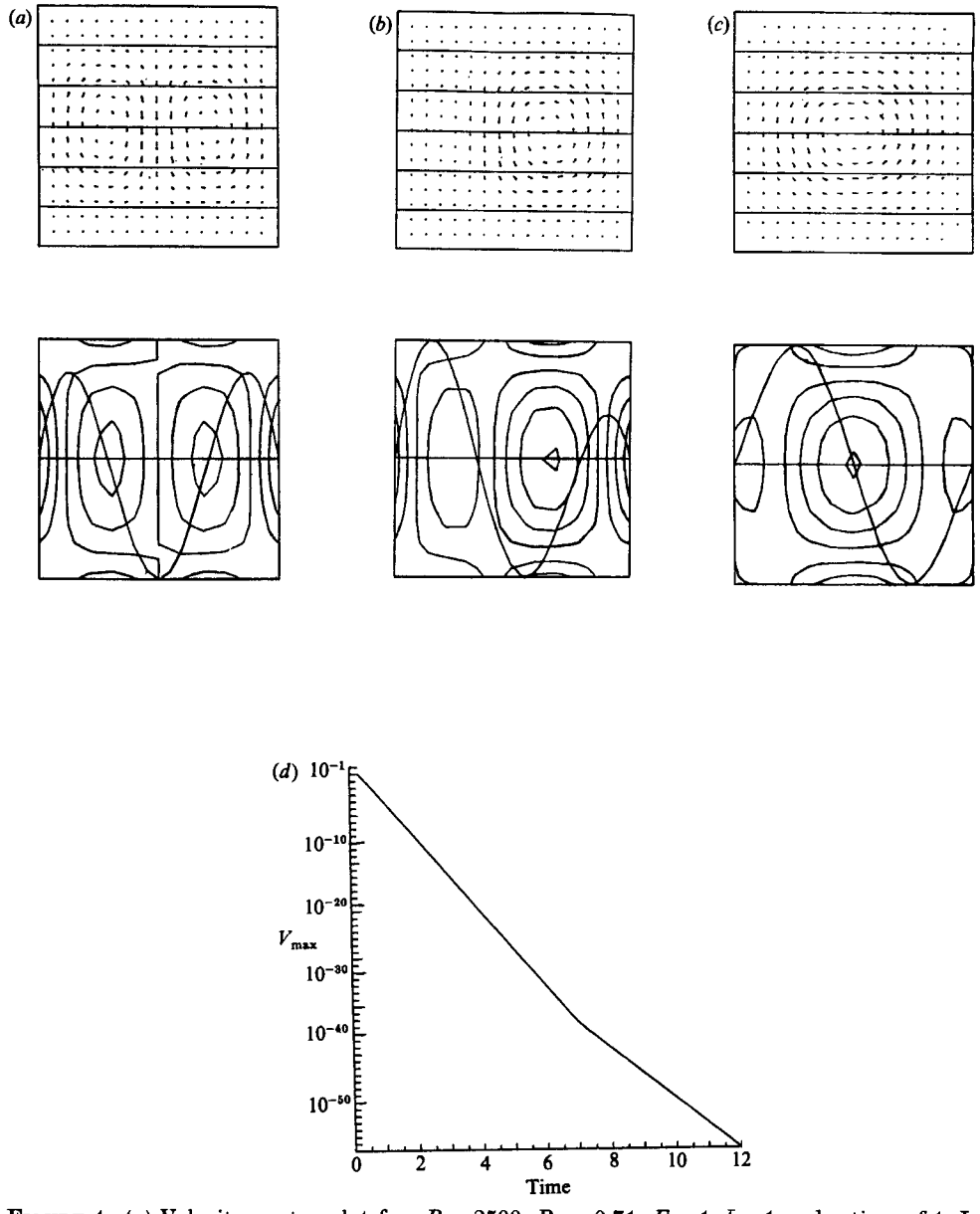

FIGURE 4. (*a*) Velocity vector plot for: $R = 2500$, $Pr = 0.71$, $\Gamma = 1$, $\bar{t} = 1$ and a time of 1. Lower plot is the corresponding vorticity contour plot with horizontal centreline temperature superimposed. (*b*) The process of breaking the reflection symmetry. The parameters are as in (*a*). The time is 6.9. (*c*) Plots as in (*a*) for a time of 12. (*d*) Maximal speed as a function of time.

a vertical line that halves the rectangle will always create an even number of rolls. An example is provided in figure 4(*a*) where two rolls have been created in a system whose Rayleigh number is 2500 and whose aspect ratio equals unity. The symmetry of the velocity and vorticity fields is obvious from the figure. During the development of the system one roll close to a sidewall will disappear and the system will stabilize to its final state. Indeed, in figure 4(*b*) we see the left roll weakened and the right roll starting to take over. The relative sizes of the rolls are even more obvious in the

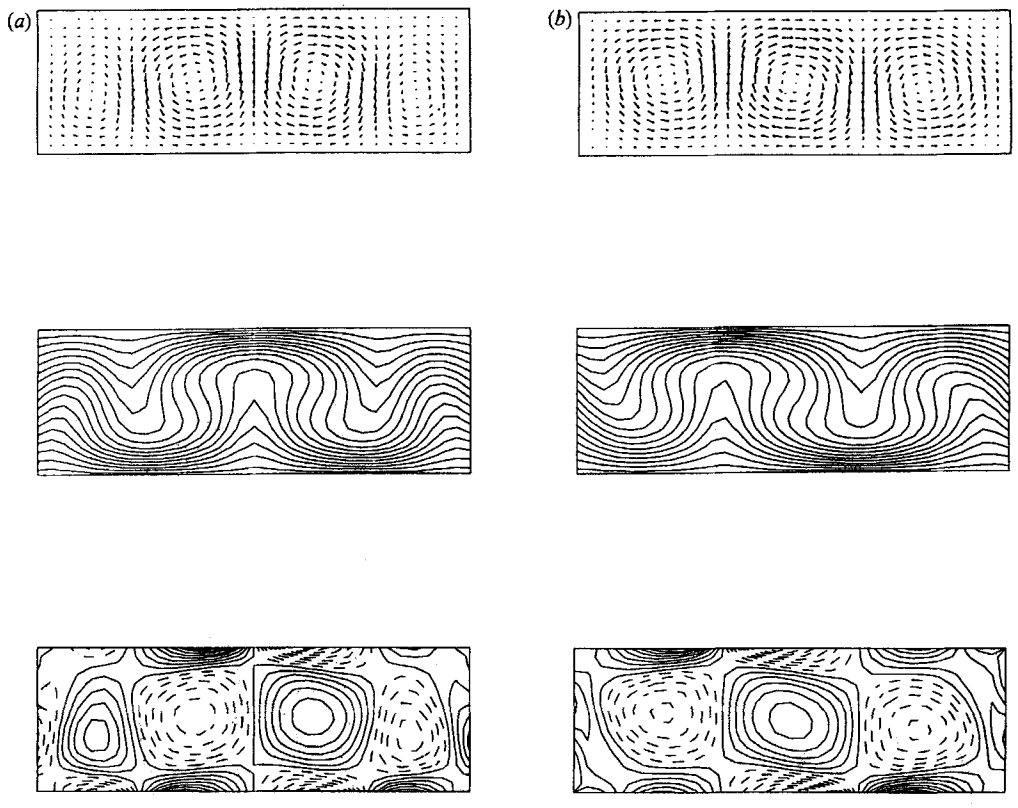

FIGURE 5. (a) Velocity vector, temperature contour and vorticity contour plots for $R = 7000$, $Pr = 0.71$, $t = 1$, $\Gamma = 3$ and a time of 1.0. No asymmetric perturbation has been used. (b) Same plots as in (a) following the application of an asymmetric perturbation.

vorticity plots. Finally in figure 4(c) we see a single roll. Since $Ra < Ra_c$ this roll will eventually decay. The transition from an even to an odd number of rolls is a symmetry breaking transition which is not possible without noise, asymmetric heating or other 'imperfections'. In our simulations, this occurs because of round-off errors or by a controlled application of an asymmetric perturbation. Figure 4(d) exhibits the transition between the two-roll state and the single-roll state as displayed by the maximal velocity in the cell as a function of time. The even number of rolls firstly decay at a faster exponential rate, then one roll disappears and the flow field decays at a slower rate. The initial slope corresponds to a decay rate of the two-roll state and the slope at later times corresponds to the decay rate of a single-roll state (whose initial amplitude was very small).

For $Ra = 7000$ and $\Gamma = 3$ we obtain a stable pattern consisting of two large rolls and two small rolls (the small rolls are the parents) both of which are in the lower (left and right) corners (see figure 5a). This state is symmetric with respect to reflection about the vertical centreline. We have tested the stability of this state by applying an asymmetric perturbation ($\beta = 0.001$ at $x_0 = z_0 = 0.25$, cf. (2.13)) to it. When a relatively large asymmetric perturbation ($\beta = 0.1$ at the same point) is applied, the system will evolve towards a stable, three-roll state as in figure 5(b). This is an example of multistability. We have also observed multistability at other Rayleigh numbers and aspect ratios.

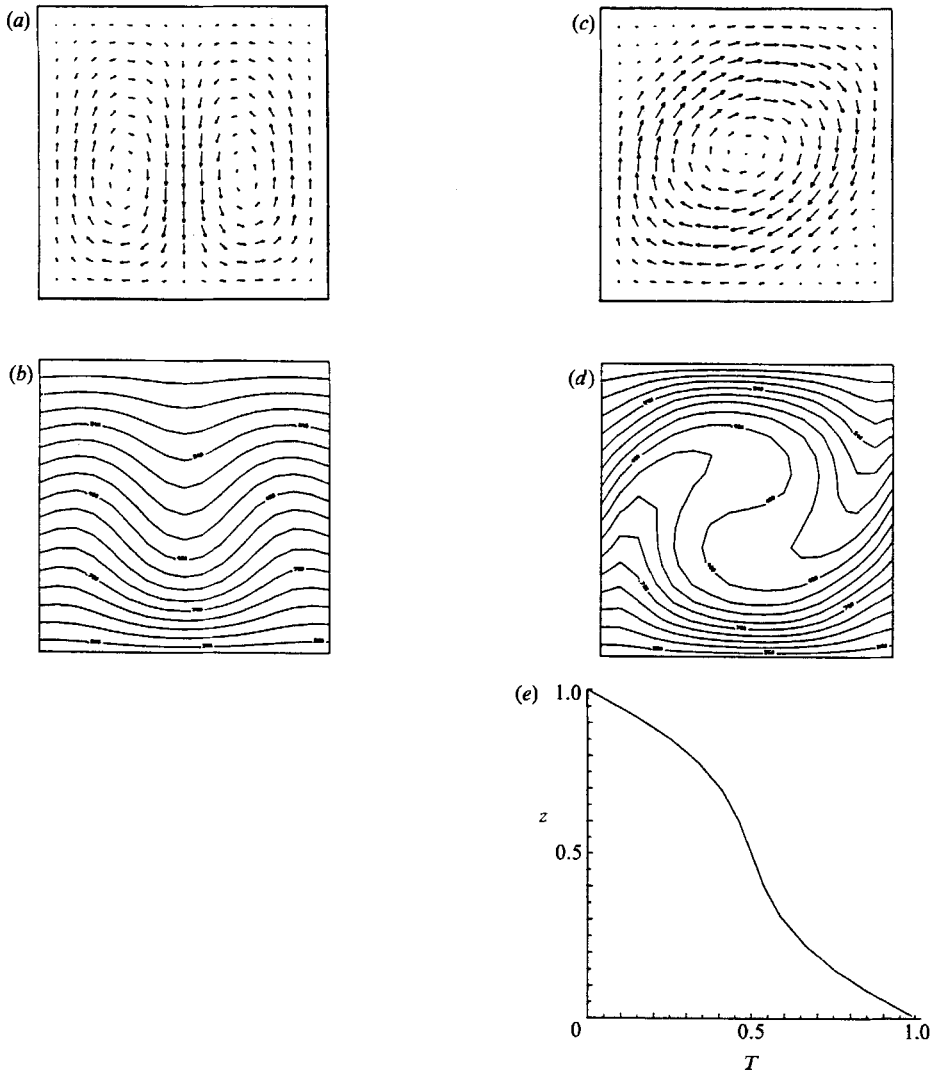

FIGURE 6. (*a*) Velocity vector plot for $R = 10000$, $Pr = 0.71$ and $\Gamma = 1$. No asymmetric perturbation has been used. (*b*) The temperature contour plot corresponding to (*a*). (*c*) Velocity vector plot corresponding to the same parameters as in (*a*). An asymmetric perturbation has been used. (*d*) Temperature contour plot corresponding to (*b*). (*e*) Horizontally averaged temperature as a function of z for $R = 50000$, $\Gamma = 1$ and $Pr = 0.71$.

In all the low-Rayleigh-number, two-dimensional simulations we have not observed any defects. Transitions between different-roll-number states proceed by eliminating rolls adjacent to the side boundaries, as we have seen before. First, a 'boundary' roll becomes weaker (lower amplitude), then it disappears altogether, and the roll adjacent to it moves in. This effect might be typically two-dimensional.

4. Intermediate Rayleigh number behaviour: $10^4 \leqslant Ra \leqslant 10^5$

In this section we present results of simulations performed at Rayleigh numbers ranging from 10000 to 100000. The creation of rolls occurs in a similar way as for low

Rayleigh numbers. The symmetric states are always metastable and long-lived in the absence of noise or perturbations. They are true (unstable) steady states of the system. In figure 6(*a*) we show a velocity plot for $Ra = 10000, \Gamma = 1$ in the absence of asymmetric perturbations. The state is symmetric with respect to the vertical centreline. Note the 'sagging' of the centres of the rolls. The effect of the large velocity pointing downward of the centreline is clearly seen in the temperature contour plot (figure 6*b*). In figure 6(*c*) we present the asymmetric steady state corresponding to the same control parameters, which was obtained using an asymmetric perturbation ($\beta = 0.1, x_0 = z_0 = 0.25, C = 32$, cf. (2.13)). Note the symmetry with respect to rotation by an angle of π, as explained in §2.1. Similar asymmetric steady states that differ only in orientation are created by different asymmetric perturbations. Similar symmetric and asymmetric steady states are obtained at higher Rayleigh numbers (up to 10^5). The boundary layers in figure 6(*d*) demonstrate the effect of mixing by the large velocity field in the centre of the cell.

At higher Rayleigh numbers ($Ra \geqslant 60000$) and aspect ratio = 1, we observe a transient 'roll-upon-roll' structure. In the final, steady, convecting state this structure is replaced by a single roll. This feature seems to be of general nature; when heating the system, it absorbs energy corresponding to a higher Rayleigh number and exhibits textures typical of such a Rayleigh number. Later, dissipation reduces the energy of the flow to that corresponding to the actual Rayleigh number. We call this the 'overshooting' effect. The effect described here has also been found in the time dependence of the Nusselt number: it first overshoots its asymptotic value, then decays to it.

At these higher Rayleigh numbers, we also start observing corner rolls. The latter become more prominent as the Rayleigh number increases. At very high Rayleigh numbers (see §5) the roll-upon-roll structure is found to be itself a stable flow solution.

In all the runs that we have described so far, the final state is steady; no time-dependent final states are observed at intermediate Rayleigh numbers, aspect ratios $\leqslant 4$ and $Pr = 0.71$.

The next series of results are for aspect ratios greater than unity. In figure 7(*a*) we see the steady velocity field for $Ra = 20000$ and $\Gamma = 2$. Note the existence of two small corner rolls. The flow field obeys the π rotation symmetry (cf. §2.1). The pattern described so far changes to a two-roll system which is symmetric about the centreline (cf. figure 7*b*) at $Ra = 50000$. The thermal boundary layer at the centre of the bottom plate (figure 7*c*) is due to the jet flowing downwards in between the rolls. This solution is stable to asymmetric perturbations. When the Rayleigh number is raised to 100000, we obtain a similar flow pattern except that the velocity field points downward at the side boundaries (see figure 7*d*). Since the initial sidewall rolls have a velocity field that points upward at the side boundaries, it is obvious that in the process that leads to this final state, the parent rolls have faded and moved into the lower corners (see the vorticity contour plot figure 7*c*). The induced rolls grow in size and become the main rolls.

The investigation of the intermediate Rayleigh numbers dynamics for $\Gamma = 4$ reveals that the number of rolls in the steady state depends on the Rayleigh number and the symmetry of the initial conditions. In figure 8(*a*) we plot the early time development of the roll structure for $Ra = 10000$ and $\Gamma = 4$. The final, six-roll, steady state is shown in figure 8(*b*). Notice that the two middle rolls are smaller in width than the other rolls. Similar patterns are found for Rayleigh numbers ranging

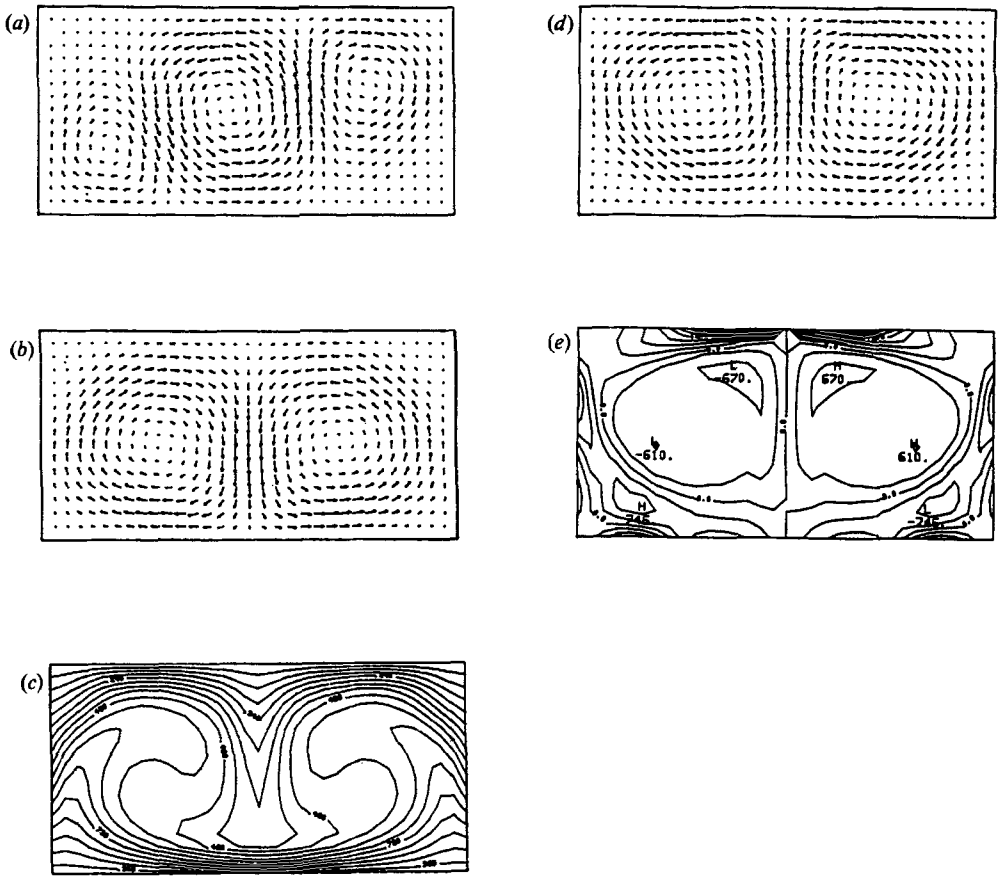

FIGURE 7. (*a*) A velocity vector plot for $R = 20000$, $\Gamma = 2$, $Pr = 0.71$ and a time of 0.5. This is a steady state. (*b*) Velocity vector plot for $R = 50000$, $Pr = 0.71$, $\Gamma = 2$ and a time of 0.5. Note that this steady state is symmetrical with respect to the vertical centreline. (*c*) Temperature contour plot corresponding to (*b*). (*d*) Velocity vector plot for $R = 100000$, $Pr = 0.71$ and $\Gamma = 2$. (*e*) Vorticity contour plot corresponding to (*d*).

to 40000. When $Ra = 50000$ the steady number of rolls reduces to four and the middle rolls are less wide than those at the sidewalls (see figure 8*c*). The corresponding temperature plot is shown in figure 8(*d*). Already at this Rayleigh number there are no significant temperature gradients outside the boundary layers, as exhibited in figure 8(*d*).

5. High Rayleigh number behaviour: $Ra \geqslant 10^5$

In this section two-dimensional convection at Rayleigh numbers higher than 10^5 is investigated. As before, we employ rigid boundary conditions at all boundaries. Flows at two Prandtl numbers, 0.71 and 6.8, are simulated.

In figure 9 we plot results for the dynamics of the Rayleigh–Bénard system in two-dimensions when the Rayleigh number is 100000 ($\approx 20 \cdot Ra_c$), the Prandtl number is 0.71, and the aspect ratio is unity. The flow develops into a periodic state (see figure 9*a* for a plot of the Nusselt number at the bottom plate, Nu, as a function of time).

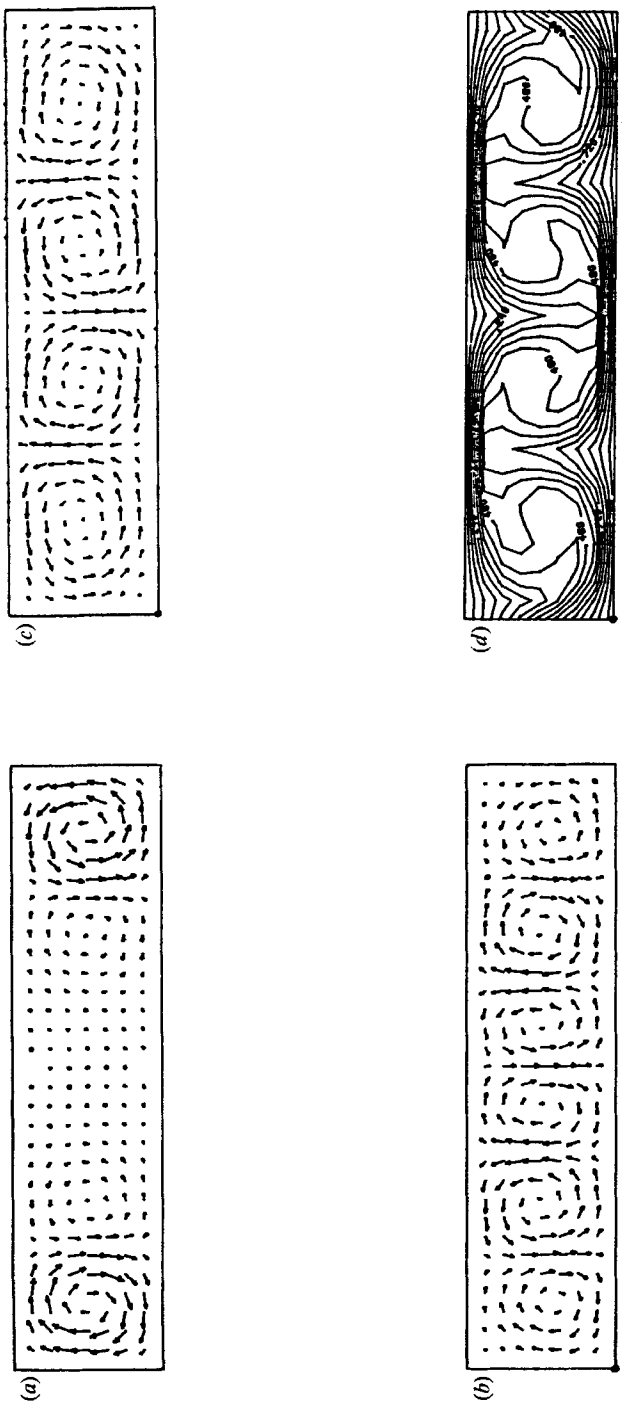

FIGURE 8. (a) Velocity vector plot for $R = 10000$, $\Gamma = 4$, $Pr = 0.71$ and a time of 0.1. (b) The steady velocity vector field of the system described in (a). (c) Steady velocity vector field for $R = 50000$, $Pr = 0.71$ and $\Gamma = 4$. (d) Temperature contour plot corresponding to (c).

In figure 9(*b–e*) we present velocity vector and temperature contour plots depicting the dynamics at two different times. A full cycle of the fluid motion consists of several stages. A fluid 'jet' (see the increased velocity of the fluid near the horizontal centreline in figure 9*b*) is moving towards the lower right-hand corner. It splits into a part co-flowing with the upper roll and a part moving towards the lower right-hand corner and then upwards. The direction of the jet changes and after half a cycle, it points towards the upper right-hand corner creating a flow field which is very much a mirror image of the previous flow field (see figure 9*d*). Later the jet returns to the state shown in figure 9*b*.

The temperature contour plots (see figure 9*c*, *e*) and the graph of the horizontally averaged temperature *vs.* z (figure 9*f*) show that the system has three boundary layers: two at the top and bottom plates and one in between the rolls. The centre part of the square cell has a very low temperature gradient due to convective mixing.

It is interesting to speculate as to the physical reason underlying the periodic motion observed in figure 9. Consider a situation in which the two main rolls are of equal strength, one upon the other and 'non-interacting'. A perturbation in the velocity field creating a slight upward motion in the right-hand part of the centreline will be subsequently amplified by the buoyancy forces. The result is a 'jet' carrying accelerating fluid towards the upper boundary. This acceleration process is terminated by the additional frictional forces which arise due to the acceleration of the upper roll as well as the flattening of the temperature gradient created by the fast jet. In the process of the jet moving upwards, the upper roll cannot absorb the full mass and momentum imparted to it by the incoming jet. Consequently, part of the fluid brought up by the jet moves towards the top right-hand corner and then moves downwards independently of the upper roll. In the upper right-hand corner there is a large temperature gradient but hardly any fluid motion, a situation that favours the increase of convective motion. The resulting shear forces will then cause the jet angle to decrease (with respect to the horizontal centreline). Inertial forces will then move the centre jet below the centreline where a process similar to the one just discussed will occur. In this way an oscillatory motion is initiated.

The physics observed at $Ra = 200000$ to 700000, $\Gamma = 1$, and $Pr = 0.71$ is similar to that at $Ra = 100000$.

An interesting change occurs in the dynamics when the Prandtl number is raised to 6.8. In figure 10 we plot results of a simulation with $Ra = 100000$ and $Pr = 6.8$. The dynamics here consists of the merging and separation of pairs of vortices. Figure 10(*a*) and the corresponding vorticity contour plot, figure 10(*b*), exhibit a state consisting of two corner vortices and a centre vortex, which had been formed by the merging of two vortices. Figure 10(*e*, *f*) depicts a later stage in the cycle which resembles the previously shown state rotated by 90°. An intermediate situation in which all four vortices are separated is found in figure 10(*c*, *d*). This process repeats *ad infinitum* and is periodic. In figure 10(*g*) the periodic behaviour of the Nusselt number is shown. We have tested the dynamics by increasing the resolution and have obtained identical results.

We have checked the dynamics for higher Rayleigh number, $Ra = 110000$–150000, and found that the period decreases, but the qualitative features of the dynamics remain the same. No frequency locking has been observed, and we believe that this kind of dynamics will continue to asymptotically large Rayleigh numbers, where further splittings and reunions of vortices are expected.

In summary, the most prominent feature of two-dimensional convection at high Rayleigh numbers ($Ra \geqslant 100000$) with rigid boundary conditions at all boundaries

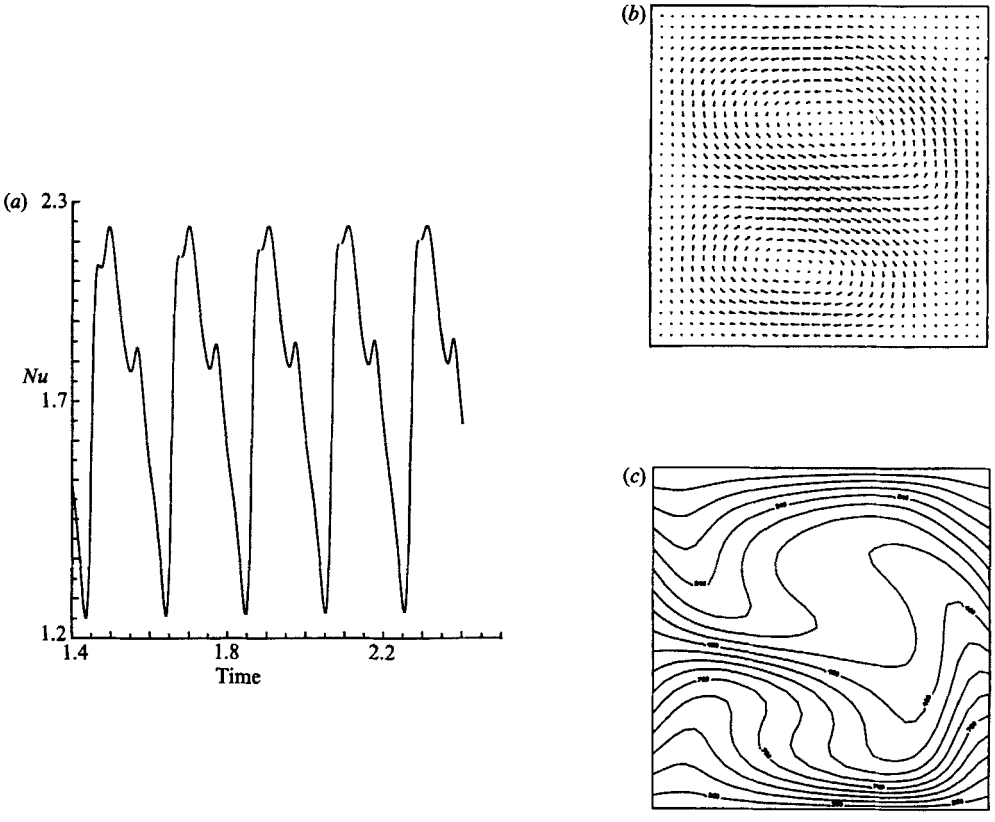

FIGURE 9(a–c). For caption see facing page.

and Prandtl number 0.71 is the surprising absence of chaotic or even quasi-periodic behaviour. This fact is to be contrasted with results obtained from low-order truncations of the two-dimensional Boussinesq equations; e.g. the Lorenz model (Lorenz 1963) or the 14-mode Curry model (Curry 1978) or from simulations in which slip or periodic boundary conditions were used (Curry *et al.* 1984). The time dependent flows here are characterized by a single frequency and its harmonics (at least up to $Ra = 10^6, Pr = 0.71$). In spite of the absence of aperiodic behaviour, these two-dimensional flows have some interesting topological flow features. For example, when the aspect ratio is unity, a time dependent roll-upon-roll state is observed. Similar flow states were observed in Hele–Shaw systems (e.g. Frick & Müller 1983; Koster & Müller 1984). The latter are, however, of different nature than pure two-dimensional convection. Corner rolls are seen in most flows, and we believe that they may generally exist but are too weak to be detected or resolved in many cases.

6. Chaotic solutions

In the present section we present evidence for the existence of chaotic dynamics when the Prandtl number is 6.8 and the Rayleigh number is large enough. This result should be contrasted with the fact that no chaotic solutions have been found when the boundary conditions are stress free or periodic (Curry *et al.* 1984). In the case of double-diffusive convection Knobloch *et al.* (1986) did obtain chaotic behaviour, but a highly resolved simulation by A. Shi & S. A. Orszag (private communication)

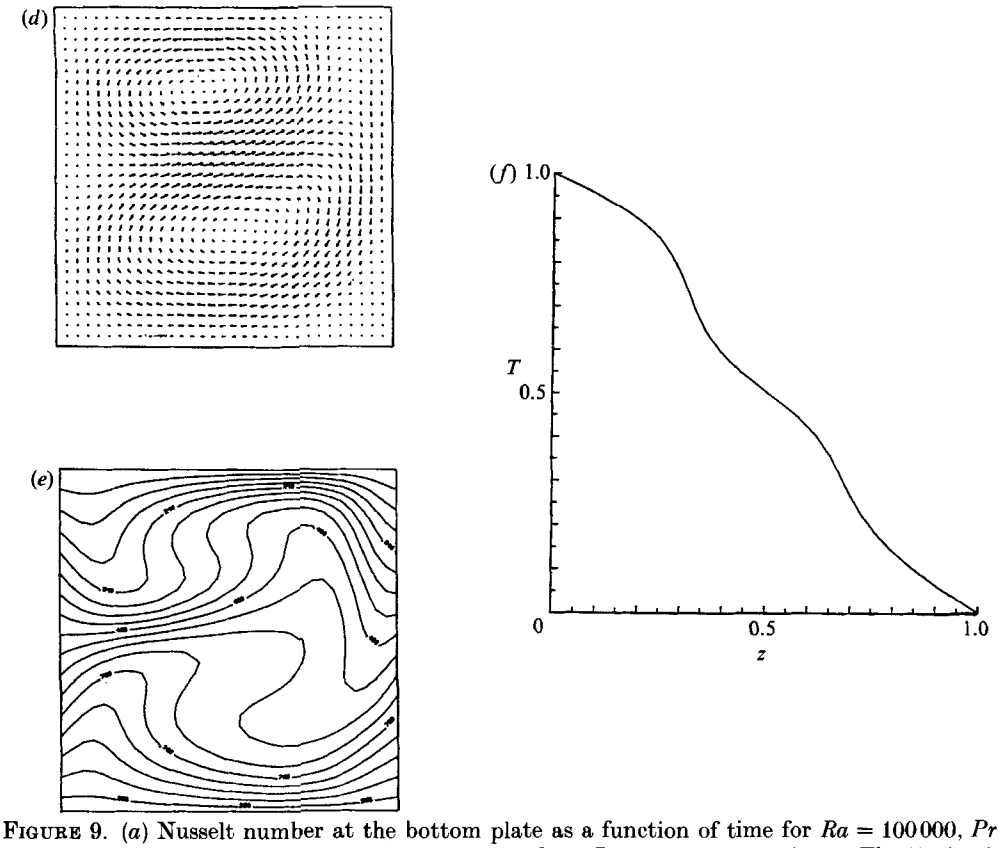

FIGURE 9. (*a*) Nusselt number at the bottom plate as a function of time for $Ra = 100000$, $Pr = 0.71$ and $\Gamma = 1$. (*b*) Velocity vector plot at a time of 1.9. Parameters are as in (*a*). The 'jet' points downwards. (*c*) Temperature contour plot corresponding to (*b*). (*d*) Velocity vector plot at time 2. Parameters are as in (*a*). (*e*) Temperature contour plot corresponding to (*d*). (*f*) Horizontally averaged temperature as a function of z. Parameters are as in (*a*).

showed that this was a result of insufficient resolution. The absence of chaotic solutions mentioned above only applies to fully resolved simulations. When a truncated set of modes (Yahata 1984; Lorenz 1963; Curry 1978) or amplitude equations (Greenside *et al.* 1982) are used, one does obtain chaotic solutions. The latter seems to be an artifact, related to the absence of sufficient damping at high k modes (which are neglected in truncations).

It seems to us that there are two major reasons for the above mentioned qualitative differences. The first is the fact that no-slip boundary conditions introduce couplings between modes that are uncoupled when slip or periodic boundary conditions are used; existent couplings are modified in a significant manner. The other reason is related to the fact that vorticity can be generated at a no-slip boundary (Siggia & Zippelius 1981). It seems that a major factor in determining whether the system will have chaotic states is the value of the Prandtl number (Schlüter, Lortz & Busse 1965; Busse 1972; Korpela, Gozum & Baxi 1973; Gershuni & Zhukhovitskii 1976).

We have learned from experience that highly restricted conditions on a system (e.g. no-slip boundary conditions, finite geometry, symmetry or finite resolution in simulation) have a tendency to delay the onset of instabilities leading to chaos as a control parameter is varied. On the other hand, such restrictions may bring about

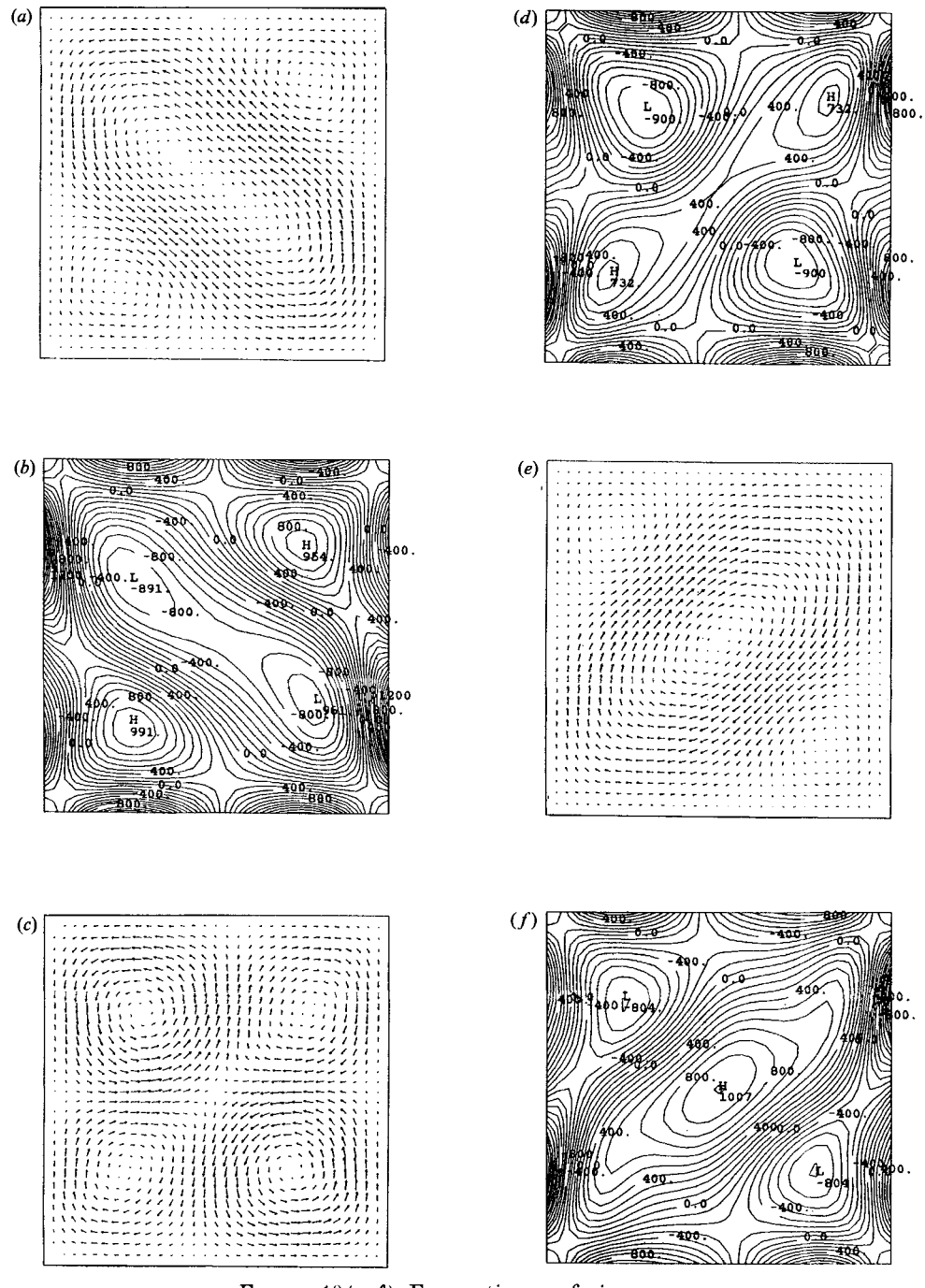

FIGURE 10(*a–f*). For caption see facing page.

chaos; without them the system might not have a chaotic state at all. Some more detailed reasoning is presented below.

As mentioned before, we have not observed any chaotic solutions at (relatively) low Γ simulations at $Pr = 0.71$, but we have observed solutions of aperiodic nature at $Pr = 6.8$. While complete physical understanding as to the reasons for the

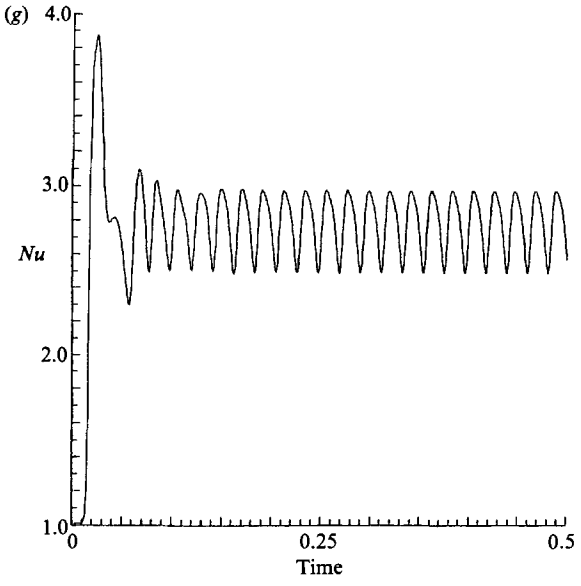

FIGURE 10. (*a*) Velocity vector field for $R = 100000$, $Pr = 6.8$, $\Gamma = 1$ and a time of 0.1. (*b*) Vorticity contour field corresponding to (*a*). (*c*) Velocity vector field, with parameters as in (*a*) at a time of 0.3. (*d*) Vorticity contour plot corresponding to (*c*). (*e*) Velocity vector field at a time of 0.5. Parameters are as in (*a*). (*f*) Vorticity contour plot corresponding to (*e*). (*g*) Nusselt number as a function of time for the cell described.

appearance of chaos at higher Pr is still lacking we wish to suggest some ideas based on our numerical results. It seems that enhanced viscosity (which corresponds to a larger Prandtl number) will increase the rate of vorticity production and will not allow large shear in the system. The latter is probably the reason why corner rolls are created and are of crucial importance in the dynamics of the flow. It appears that there is a constant competition between the corner rolls and the other rolls. Sometimes the corner rolls grow in size at the expense of the other rolls and sometimes the opposite will happen. This 'pattern competition' (Busse & Clever 1979; Ciliberto & Gollub 1984; Bolton, Busse & Clever 1986) is presumably responsible (or partly responsible) for the observed chaotic behaviour.

In figure 11 we demonstrate the dynamics of the two-dimensional Boussinesq equations for $\Gamma = 2$, $Pr = 6.8$ and $Ra = 100000$. Figure 11 (*a–h*) exhibits velocity vector and vorticity contour plots for this system, from a time of 1.57 to 3.32. These plots represent the 'fully developed dynamics'. By this time the transient states seem to have decayed. The latter was tested by doubling the number of collocation points in each direction (32^2 to 64^2).

The higher resolved dynamics, which is not reproduced here, is almost identical to that obtained using the lower resolution. Due to limitations in computer resources, the latter runs were made for a shorter time than the former, yielding, as mentioned above, equivalent results, e.g. spectra. Unless the chaos decays after a very long time, a possibility in every numerically or experimentally obtained chaotic state, we believe we have obtained true chaotic dynamics.

As seen in figure 11, the number of rolls in the box is changing from 3 major rolls (figure 11*b*) to 6 (figure 11*h*). A close inspection of the corresponding vorticity contour plots reveals the existence of additional, smaller rolls near the corners. The

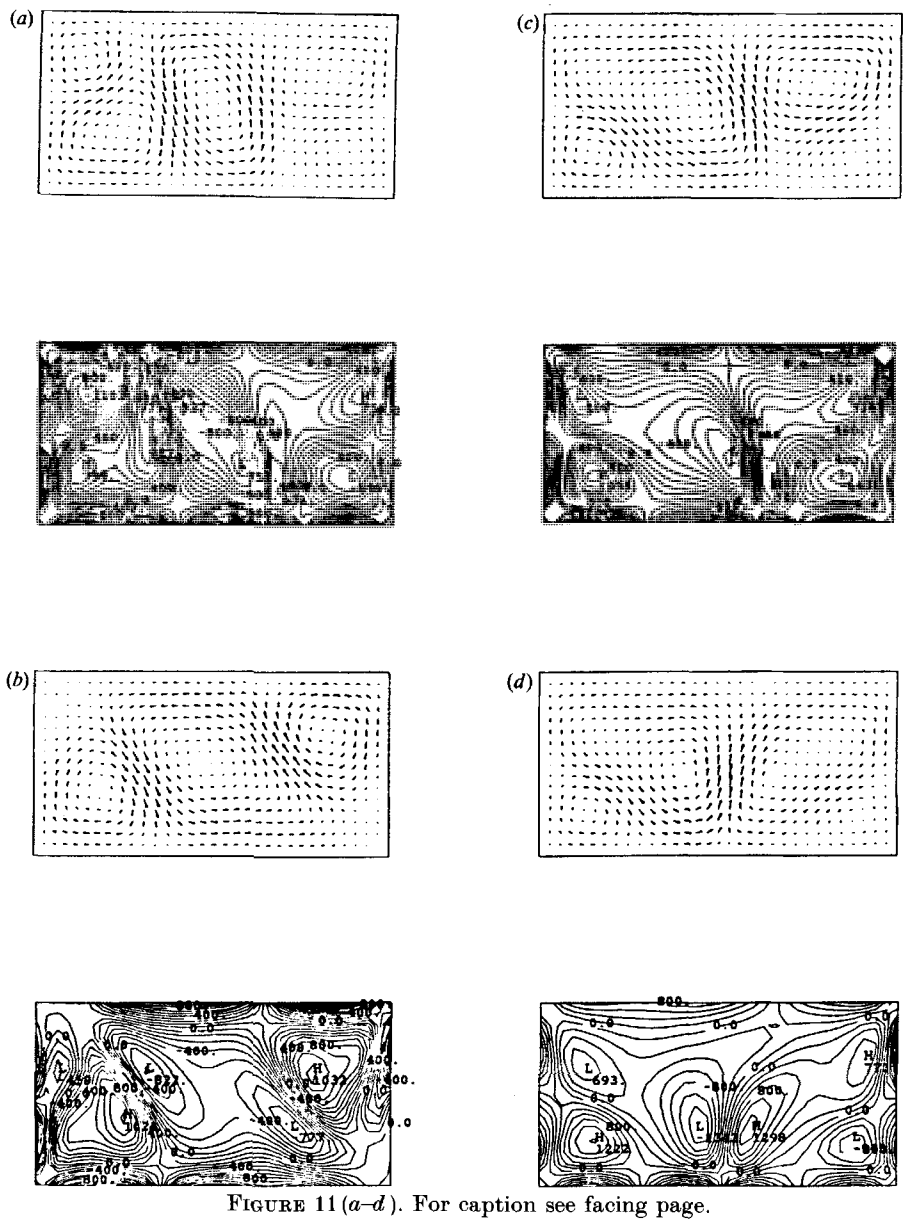

FIGURE 11 (*a–d*). For caption see facing page.

rolls may grow in size and merge with larger rolls as is seen at a time of 2.07 (figure 11*c*). Note the existence of large vorticity gradients at the boundaries and in between the rolls. The time difference between consecutive plots is too large to follow the continuous dynamics of the system; they are merely samples of the possible states of the system. In each plot there are one or two 'jets'; we recall in §5 that such jets were of importance in the periodic dynamics.

In many of the flow states we have observed 'quasi-triangular' rolls, which normally have two extrema in their vorticity (see e.g. figure 11*f*). They are composed of pairs of co-rotating vortices which match by having the velocity at their 'interface' vanish (see §5).

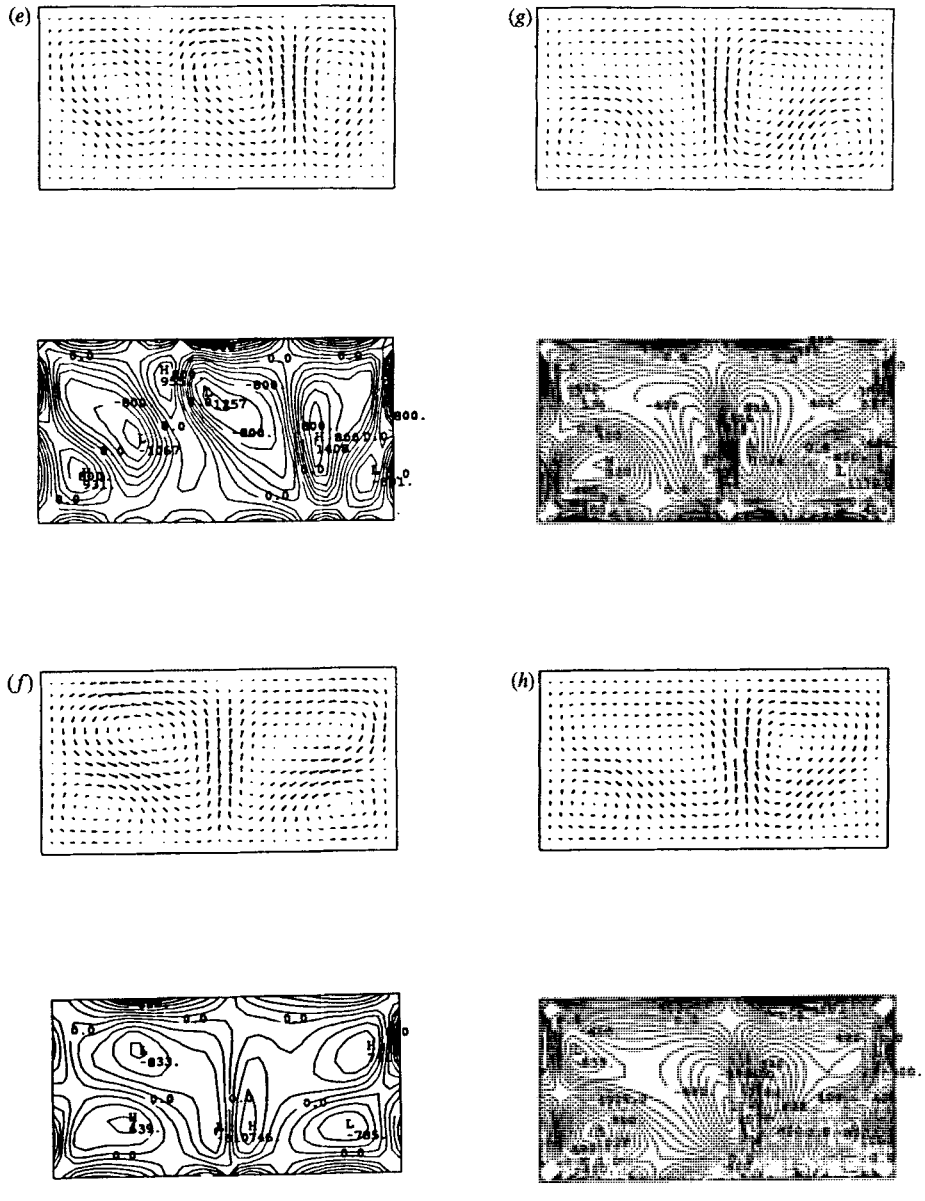

FIGURE 11. Velocity vector and corresponding vorticity contour plots for $\Gamma = 2$, $Pr = 6.8$ and $Ra = 100000$ at the following times: (*a*) 1.57; (*b*) 1.82; (*c*) 2.07; (*d*) 2.32; (*e*) 2.57; (*f*) 2.82; (*g*) 3.07; (*h*) 3.32.

In figure 12(*a*) we present a plot of the Nusselt number at the bottom plate as a function of time. It seems to be aperiodic. The corresponding correlation function for the Nusselt number is presented in figure 12(*b*). The non-decaying nature of this correlation is attributed to the fact that the chaotic part of the correlation is superimposed on a quasi-periodic part. Figure 12(*c*), a plot of the power spectrum of Nusselt number, shows the existence of a fundamental mode with a frequency of about 155 and its harmonic (denoted by arrows). The power spectrum is broad and similar to other power spectra corresponding to chaotic series. Figure 12(*d*) presents

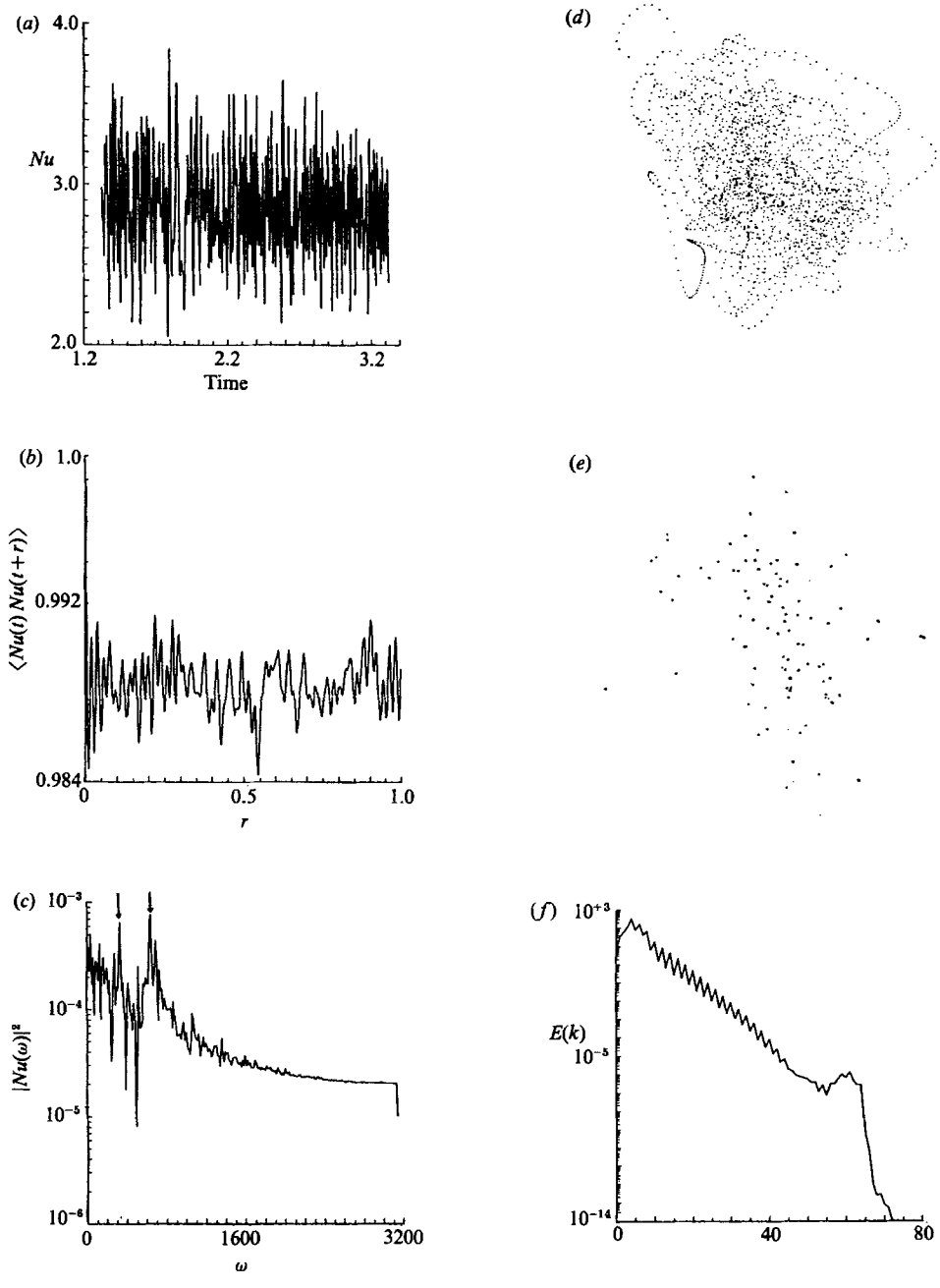

FIGURE 12. (*a*) Nusselt number at the bottom plate as a function of time. (*b*) Correlation function corresponding to (*a*). (*c*) Power spectrum of the Nusselt number corresponding to the time series in (*a*). (*d*) Phase space plot of corresponding to the Nusselt number at the bottom plate. Plotted is $Nu(t+\tau)$ *vs.* $Nu(t)$ for $\tau = 0.01$. (*e*) Poincaré section corresponding to the Nusselt number at the bottom plate. The plotted points are $Nu(t+\tau)$ *vs.* $Nu(t+2\tau)$ when $Nu(t) = 2.8$. (*f*) Spatial energy spectrum as a function of wavenumber at a time of 0.36.

a phase space plot corresponding to the Nusselt number at the bottom plate. The discreteness of the points in the phase space plot is due to the fact that our numerical procedure is performed in discretized time. The delay time used in these plots is 0.01, which is about half the typical oscillation period of the system. Other delay times yielded similar results. The phase space plot was computed from a single signal using an embedding method which is frequently employed in the literature (Takens 1981*a*, *b*; Grassberger & Procaccia 1983). Figure 12(*e*) presents a Poincaré section (Guckenheimer & Holmes 1983) corresponding to the Nusselt number at the bottom plate. In spite of the poor statistics (which is due to the very large computational time necessary to generate a point in the Poincaré section) it is evident that the system is not quasi-periodic. The correlation dimension (Grassberger & Procaccia 1983; Malraison *et al.* 1983) of the above described state is approximately 2.2.

We have tested the accuracy of our solution by computing the energy spectrum as a function of k (see figure 12*f*). Indeed, as this plot shows, the energy contained in the resolved modes decays by about 8 orders of magnitude from the lowest to highest k-mode. We have no explanation of the small hump observed at high k. However, due to its very small magnitude, we do not believe it to be dynamically important. The rate of dissipation in the same range of k-vectors has been found to decay by over 3 orders of magnitude. The true number of modes participating in the dynamics is thus very low (in three dimensions, cf. Gollub & McCarriar 1982; Gollub, McCarriar & Steinman 1982).

7. Conclusions

The effect of boundary conditions on the nature of the flow and temperature fields of the Rayleigh–Bénard system in two space dimensions has been demonstrated. It has been shown that, on one hand, the imposition of no-slip boundary conditions at all boundaries suppresses flows whose time dependence is more complex than periodic for $Pr = 0.71$, unlike the case of less realistic periodic or frec-slip boundary conditions. On the other hand, the same rigid boundary conditions give rise to chaotic flows when the Prandtl number is 6.8, whereas no such effect has been observed for periodic or free-slip boundary conditions. We thus see that for relatively low Prandtl numbers, no-slip boundary conditions have a strong controlling effect on the complexity of the flow. For higher Prandtl number it seems that additional couplings between various modes as well as vorticity creation at the boundaries, both of which result from the no-slip condition, are responsible for the creation of chaotic states.

The process of initiation of the convective flows has been investigated. We have shown how boundary heating, which is necessary to achieve a given Rayleigh number leads to the creation of rolls near the side boundaries. The latter may then move into the interior of the cell and/or induce additional adjacent rolls, depending on the parameters characterizing the preparation of the system. This effect is observed even well below the critical Rayleigh number.

Symmetries and symmetry breaking are important for the flow pattern selection in the system. Since our 'process' of heating shares some of the symmetries of the (Boussinesq) equations of motion we have obtained metastable symmetric flow states. Some of these states are stable to small perturbations but would develop into asymmetric states when perturbed by a strong perturbation. Others are relatively unstable and our numerical roundoff errors are sufficient to drive them towards their respective stable, asymmetric, final states. Some final states are truly symmetric.

We have seen that even time periodic states can possess complex flow patterns. Some of these periodic states would involve merging and separation of vortices. Others would involve a slight 'jitter' of nearby rolls. An interesting state has been observed for an aspect ratio of unity and a Prandtl number of 0.71: a roll-upon-roll state. The rolls observed in most of our simulations are relatively distorted, the distortion growing with the Rayleigh number. Some rolls would stay almost permanently near the corners and we termed these corner rolls. The latter seem to 'fill gaps' which are not accessible to the 'main' relatively large rolls. The chaotic state (for $\Gamma = 2$) involves, most of the time, five highly distorted rolls. Thus the topology and morphology of the flow pattern at the relatively low aspect ratios we have studied possess much more structure than one would expect on the basis of amplitude equations or results pertaining to high-aspect-ratio systems.

The number of modes 'participating' in all of these interesting dynamical effects is very low and comprises at most one decade in wave-vector space. Consequently, the hydrodynamic system we have considered may correspond to a rather simple dynamical system. This correspondence as well as the properties of the chaotic state will be described in detail in future work.

This work was supported by the Israel–United States Binational Science Foundation (Grant 84-00073), the National Science Foundation under Grant ATM 84-14410 and Grant DMS 8411169, the Office of Naval Research under Contract N00014-85-K-0201, and the Control Data Corporation for a Pacer Fellowship (R.B.P.). We should also like to thank the National Center for Atmospheric Research, which is sponsored by the National Science Foundation, for the computing time used in this research.

REFERENCES

AHLERS, G. & BEHRINGER, R. P. 1978 The Rayleigh–Bénard instability and the evolution of turbulence. *Prog. Theor. Phys. Supp.* **64**, 186–201.

AHLERS, G., CROSS, M. C., HOHENBERG, P. C. & SAFRAN, S. 1981 The amplitude equation near the convective threshold: application to time-dependent heating experiments. *J. Fluid Mech.* **110**, 297–334.

BOLTON, E. W., BUSSE, F. H. & CLEVER, R. M. 1986 Oscillatory instabilities of convective rolls at intermediate Prandtl numbers. *J. Fluid Mech.* **164**, 469–485.

BOUSSINESQ, J. 1903 *Théorie Analytique de Chaleur*, vol. 2, p. 172. Paris: Gauthier-Villars.

BUSSE, F. F. 1972 The oscillatory instability of convection rolls in a low Prandtl number fluid. *J. Fluid Mech.* **52**, 97–112.

BUSSE, F. H. 1978 Nonlinear properties of thermal convection. *Rep. Prog. Phys.* **41**, 1929.

BUSSE, F. H. & CLEVER, R. M. 1979 Instabilities of convection rolls in a fluid of moderate Prandtl number. *J. Fluid Mech.* **91**, 319–335.

BUSSE, F. H. & FRICK, H. 1985 Square pattern convection in fluids with strongly temperature dependent viscosity. *J. Fluid Mech.* **150**, 451–465.

CHANDRASEKHAR, S. 1961 *Hydrodynamic and Hydromagnetic Stability*. Oxford University Press.

CILIBERTO, S. & GOLLUB, J. P. 1984 Pattern competition leads to chaos. *Phys. Rev. Lett.* **52**, 922.

CROSS, M. C. 1982*a* Ingredients of a theory of convective textures close to onset. *Phys. Rev.* A **25**, 1065–1076.

CROSS, M. C. 1982*b* Wave-number selection by soft boundaries near threshold. *Phys. Rev.* A **29**, 391–392.

CROSS, M. C., DANIELS, P. G., HOHENBERG, P. C. & SIGGIA, E. D. 1980 Effect of distant sidewalls on wave-number selection in Rayleigh–Bénard convection. *Phys. Rev. Lett.* **45**, 898–901.

CROSS, M. C., DANIELS, P. G., HOHENBERG, P. C. & SIGGIA, E. D. 1983*a* Phase-winding solutions in a finite container above the convective threshold. *J. Fluid Mech.* **127**, 155–183.

CROSS, M. C., HOHENBERG, P. C. & LÜCKE, M. 1983*b* Forcing of convection due to time-dependent heating near threshold. *J. Fluid Mech.* **136**, 155–183.

CROSS, M. C. & NEWELL, A. C. 1984 Convective patterns in large aspect ratio systems. *Physica* **10** D, 299–328.

CURRY, J. H. 1978 A generalized Lorenz system. *Comm. Math. Phys.* **60**, 193–204.

CURRY, J. C., HERRING, J. R., LONCARIC, J. & ORSZAG, S. A. 1984 Order and disorder in two- and three-dimensional Bénard convection. *J. Fluid Mech.* **147**, 1–38.

CVITANOVIC, P. 1984 *Universality in Chaos.* Bristol: Adam Hilger.

FRICK, H. & MÜLLER, U. 1983 Oscillatory Hele-Shaw convection. *J. Fluid Mech.* **126**, 521–532.

GERSHUNI, G. Z. & ZHUKHOVITSKII 1976 *Convective Stability of Incompressible Fluids.* Jerusalem: Keter.

GIGLIO, M., MUSAZZI, S. & PERINI, U. 1981 Transition to chaotic behaviour via a reproducible sequence of period doubling bifurcations. *Phys. Rev. Lett.* **47**, 243–246.

GOLLUB, J. P. & BENSON, S. V. 1980 Many routes to turbulent convection. *J. Fluid Mech.* **100**, 449–470.

GOLLUB, J. P. & MCCARRIAR, A. R. 1982 Convection patterns in Fourier space. *Phys. Rev.* A **26**, 3470–3476.

GOLLUB, J. P., MCCARRIAR, A. R. & STEINMAN, J. F. 1982 Convective pattern evolution and secondary instabilities. *J. Fluid Mech.* **125**, 259–281.

GOTLIEB, D. & ORSZAG, S. A. 1977 *Numerical Analysis of Spectral Methods: Theory and Applications.* SIAM, Philadelphia.

GRASSBERGER, P. & PROCACCIA, I. 1983 Characterization of strange attractors. *Phys. Rev. Lett.* **50**, 346.

GREENSIDE, H. S., AHLERS, G., HOHENBERG, P. C. & WALDEN, R. W. 1982 A simple stochastic model for the onset of turbulence in Rayleigh–Bénard convection. *Physica* **5** D, 322–334.

GREENSIDE, H. S., COUGHRAN JR., W. M. & SCHRYER, N. L. 1982 Nonlinear pattern formation near the onset of Rayleigh–Bénard convection. *Phys. Rev. Lett.* **49**, 726–729.

GRÖTZBACH, G. 1982 Direct numerical simulation of laminar and turbulent Bénard convection. *J. Fluid Mech.* **119**, 27–53.

GRÖTZBACH, G. 1983 Spatial resolution requirement for direct numerical simulation of Rayleigh–Bénard convection. *J. Comp. Phys.* **49**, 241–264.

GUCKENHEIMER, J. & HOLMES, P. 1983 *Nonlinear Oscillations, Dynamical Systems and Bifurcations of Vector Fields.* Springer.

HAIDVOGEL, D. B. & ZANG, T. 1979 The accurate solution of Poisson's equation by expansion in Chebyshev polynomials. *J. Comp. Phys.* **30**, 167–180.

KNOBLOCH, E., MOORE, D. R., TOOMRE, J. & WEISS, N. O. 1986 Transitions to chaos in two-dimensional double-diffusive convection. *J. Fluid Mech.* **166**, 409–448.

KORPELA, S. A., GOZUM, D. & BAXI, C. B. 1973 *Intl J. Heat Mass Transfer* **16**, 1683.

KOSTER, J. N. & MÜLLER, U. 1984 Oscillatory convection in vertical slots. *J. Fluid Mech.* **139**, 363–390.

LIBCHABER, A. & MAURER, J. 1980 Une expérience de Rayleigh–Bénard de géométrie réduite; multiplication, accrochage et démultiplication de fréquences. *J. Phys. (Paris)* **41** Colloque C3, 51–56.

LORENZ, E. N. 1963 Deterministic nonperiodic flow. *J. Atmos. Sci.* **20**, 130.

MCLAUGHLIN, J. B. & ORSZAG, S. A. 1982 Transition from periodic to chaotic thermal convection. *J. Fluid Mech.* **122**, 123–142.

MALRAISON, B., ATTEN, P., BERGE, P. & DUBOIS, M. 1983 Dimension of strange attractors: an experimental determination for the chaotic regime of two convective systems. *J. Physique Lett.* **44**, L-897–L-902.

MOORE, D. R. & WEISS, N. O. 1973 Two-dimensional Rayleigh–Bénard convection. *J. Fluid Mech.* **58**, 289–312.

NEWELL, A. C. & WHITEHEAD, J. A. 1969 Finite bandwidth, finite amplitude convection. *J. Fluid Mech.* **38**, 279–303.

ORSZAG, S. A., ISRAELI, M. & DEVILLE, M. O. 1986 Boundary conditions for incompressible flows. *J. Sci. Comp.* **1**, 75–111.

ORSZAG, S. A. & PATERA, P. T. 1983 Secondary instability of wall-bounded shear flows. *J. Fluid Mech.* **128**, 347–385.

SCHLÜTER, A., LORTZ, D. & BUSSE, F. 1965 On the stability of steady finite amplitude convection. *J. Fluid Mech.* **35**, 129–144.

SEGEL, L. 1969 Distant side walls cause slow modulation of cellular convection. *J. Fluid Mech.* **38**, 203–224.

SIGGIA, E. D. & ZIPPELIUS, A. 1981*a* Dynamics of defects in Rayleigh–Bénard convection. *Phys. Rev.* A **24**, 1036–1049.

SIGGIA, E. D. & ZIPPELIUS, A. 1981*b* Pattern selection in Rayleigh–Bénard convection near threshold. *Phys. Rev. Lett.* **47**, 835.

TAKENS, F. 1981*a* In *Proc. Symp. on Dynamical Systems and Turbulence, University of Warwick, 1979–80* (ed. D. A. Rand & L. S. Young). Springer.

TAKENS, F. 1981*b* Invariants related to dimension and entropy. *Proc. 13th Brazilian Colloquium on Mathematics* (unpublished).

YAHATA, H. 1984 Onset of chaos in the Rayleigh–Bénard convection. *Prog. Theor. Phys. Supp.* **79**, 26–74.

ZIPPELIUS, A. & SIGGIA, E. D. 1982 Disappearance of stable convection between free-slip boundaries. *Phys. Rev.* A **26**, 1788–1790.